Dominant Modes of Wintertime Upper-Tropospheric Temperature Variations over Asia and Links to Surface Climate

XINGWEN JIANG,* SONG YANG,+ YUEQING LI,* ZONGJIAN KE,# JIANPING LI,@ AND HAORAN HU*

* *Institute of Plateau Meteorology, China Meteorological Administration, Chengdu, China*
+ *Department of Atmospheric Sciences, Sun Yat-sen University, Guangzhou, China*
# *National Climate Center, China Meteorological Administration, Beijing, China*
@ *National Key Laboratory of Atmospheric Sciences and Geophysical Fluid Dynamics, Institute of Atmospheric Physics, Chinese Academy of Sciences, Beijing, China*

(Manuscript received 5 November 2012, in final form 3 June 2013)

ABSTRACT

In this study, the authors investigate the variations and predictability of wintertime upper-tropospheric temperature (UTT) over Asia, which are often linked to severe climate anomalies, and the associated features of large-scale circulation and surface climate. The ECMWF Interim Re-Analysis (ERA-Interim) and hindcast of the NCEP Climate Forecast System, version 2 (CFSv2), are mainly analyzed.

The first empirical orthogonal function mode of UTT shows a dipole structure, with a strong positive center over southern China and a weak negative center over Mongolia. The second mode is featured by a monopole variation, with a positive center appearing from the northwestern Tibetan Plateau (TP) to Japan. The third mode exhibits a tripole pattern, with two positive centers over Pakistan and the Sea of Japan and a negative center over central Asia. The first mode is linked to El Niño–Southern Oscillation, accompanied by surface warming over the southeastern TP and deficient precipitation over southern China, the Korean Peninsula, and from equatorial East Africa to the east of the TP. The second mode is associated with circulation anomalies similar to those associated with the Arctic Oscillation, with significant warming over East Asia. The third mode features two wave trains and is linked to the Middle East jet stream, and is associated with excessive precipitation from the eastern TP to southern Japan. The CFSv2 can predict the first mode skillfully by several months in advance, but it shows little skill in predicting the second and third modes.

1. Introduction

The Asian monsoon (AM) is the strongest component of the global monsoon system (Webster et al. 1998; Chang 2004). Large-scale land–sea thermal contrast is generally considered as the driving force for the AM (Webster et al. 1998; Chou 2003; Wu et al. 2012). The variations of AM are closely related to the variability of the tropospheric temperature (TT) on a wide range of time scales (Li and Yanai 1996; Liu and Yanai 2001; Zhao et al. 2010; Zuo et al. 2012). A strong (weak) Asian summer monsoon is associated with positive (negative) TT anomalies over Eurasia, but negative (positive) TT anomalies over the Indian Ocean and the eastern Pacific (Li and Yanai 1996). The weakening trend in large-scale Asian summer monsoon circulation may be ascribed to the relatively smaller warming over Asia compared to the surrounding regions (Zuo et al. 2012). The tendency of increased droughts in northern China and more floods along the Yangtze River valley is due partly to the strong cooling trend in the upper-tropospheric temperature (UTT) over East Asia in July and August during the period from 1950 to 2000 (Yu et al. 2004). In addition to the local climate impact of TT over Asia, Nan et al. (2009) reported a remote influence of springtime UTT over the Tibetan Plateau (TP) on the evolution of sea surface temperature (SST) over the tropical central-eastern Pacific in spring and summer.

Given the important role of TT in the AM, previous effort has been devoted to exploring the characteristics and mechanisms of TT variations over Asia. Zhao et al. (2007b) reported that the variability of summertime eddy UTT, defined as the difference between UTT and

Corresponding author address: Prof. Song Yang, Department of Atmospheric Sciences, Sun Yat-sen University, 135 W Xingang Road, Haizhu District, Guangzhou, Guangdong 510275, China.
E-mail: yangsong3@mail.sysu.edu.cn

DOI: 10.1175/JCLI-D-12-00774.1

its zonal mean, was out of phase between Asia and the North Pacific, and was accompanied by different rainfall anomalies over Asia and the western Pacific. The summer UTT over East Asia has two distinct modes: a monopole pattern and a meridional dipole pattern. The variation of TT was attributed to either local heating (e.g., the sensible heating over the TP) or remote forcing from the tropical convection (Li and Yanai 1996; Tamura et al. 2010; Jiang et al. 2011; Zhang and Zhou 2012).

There is increasing evidence indicating that the close relationship between Asian climate and TT occurs not only during spring and summer, but also during winter. Previous studies have indicated that the severe droughts in northern China in winter 2008/09 and southern China from January to May in 2011 were partially ascribed to the increase in TT over the TP (Gao and Yang 2009; Sun and Yang 2012). For the drought in winter 2008/09, the higher-than-normal surface temperature and TT over the TP favored a shallow India–Burma trough, contributing to weak transportation of water vapor to northern China (Gao and Yang 2009). In spite of the potential climate impact of winter TT over Asia, its variations are not fully known.

The recent winter extreme climate anomalies over China are accompanied by not only the TT anomalies over the TP, but also the anomalies of other climate phenomena such as El Niño–Southern Oscillation (ENSO) and North Atlantic Oscillation (NAO) (Gao and Yang 2009; Sun and Yang 2012). Zhang and Zhou (2012) reported that the UTT anomalies over East Asia were associated with ENSO and exhibited different patterns during ENSO developing and decaying summers. Are the wintertime TT anomalies also linked to ENSO and the other climate phenomena?

In this study, we focus on the interannual variation of wintertime TT over Asia, aiming at the following questions: Are there distinct modes of the interannual variation of winter TT over Asia? If so, what are the circulation anomalies associated with the most dominant modes? How are these modes linked to the variations of surface climate anomalies and their impacting factors? We also assess the skill of prediction of these dominant modes by the National Centers for Environmental Prediction (NCEP) Climate Forecast System, version 2 (CFSv2). It has been demonstrated that the CFSv2 is skillful in predicting the Asian summer monsoon and winter monsoon (Jiang et al. 2013a,b). However, how well the model can predict the dominant modes of wintertime TT over Asia is not yet known.

The rest of this paper is organized as follows. Descriptions of data, analysis methods, and the CFSv2 are given in section 2. Several dominant modes of the interannual variations of wintertime UTT over Asia are discussed in section 3. In section 4, we investigate the large-scale circulation features associated with the three leading modes and their differences from the features related to other climate patterns. In section 5, we discuss the surface climate anomalies associated with the leading modes. We assess the skill of prediction of the dominant modes of winter UTT by CFSv2 in section 6. A summary and discussion of the results obtained are provided in section 7.

2. Data, analysis methods, and model

The datasets used in this study include the European Centre for Medium-Range Weather Forecast (ECMWF) Interim Reanalysis (ERA-Interim; Dee et al. 2011), from which monthly mean geopotential height and winds at 12 pressure levels (1000, 925, 850, 700, 600, 500, 400, 300, 250, 200, 150, and 100 hPa), surface air temperature, and sea level pressure (SLP) are analyzed. The reanalysis is in resolution of 0.75° (latitude) × 0.75° (longitude). The period of 1982–2010 is used in the study to be comparable with the CFSv2 hindcast. The monthly mean SST from the National Oceanic and Atmospheric Administration (NOAA) optimum interpolation SST (OISST) analysis (Reynolds et al. 2007) and the monthly mean rainfall from the NOAA Climate Prediction Center (CPC) Merged Analysis of Precipitation (CMAP; Xie and Arkin 1997) are also analyzed. For validation of the analysis data, precipitation and surface air temperature for 668 China stations from the National Climate Center of the China Meteorological Administration are also applied. The Arctic Oscillation (AO) index and the NAO index are obtained from the NOAA Climate Prediction Center at http://www.cpc.ncep.noaa.gov/products/precip/CWlink/daily_ao_index/monthly.ao.index.b50.current.ascii and http://www.cpc.ncep.noaa.gov/products/precip/CWlink/pna/norm.nao.monthly.b5001.current.ascii, respectively. We also employ another AO index (Li and Wang 2003a) and NAO index (Li and Wang 2003b; Li 2005), which can be downloaded (at http://ljp.lasg.ac.cn/dct/page/65569 and http://ljp.lasg.ac.cn/dct/page/65574, respectively) to verify the results from the indices mentioned above. The fact that the same conclusion was obtained implies that the results here are not index dependent.

We also apply several other indices, including the Siberian high (SH), defined as the averaged SLP over 40°–60°N, 70°–120°E (Gong et al. 2001); the East Asian jet stream (EAJS) index, defined as the areal mean of 200-hPa zonal wind over 30°–35°N, 130°–160°E (Yang et al. 2002); and the Middle East jet stream (MEJS) index defined as the difference in 200-hPa zonal wind between 20°–30°N, 40°–70°E and 30°–40°N, 15°–45°E (Yang et al. 2004). The East Asian trough (EAT) is

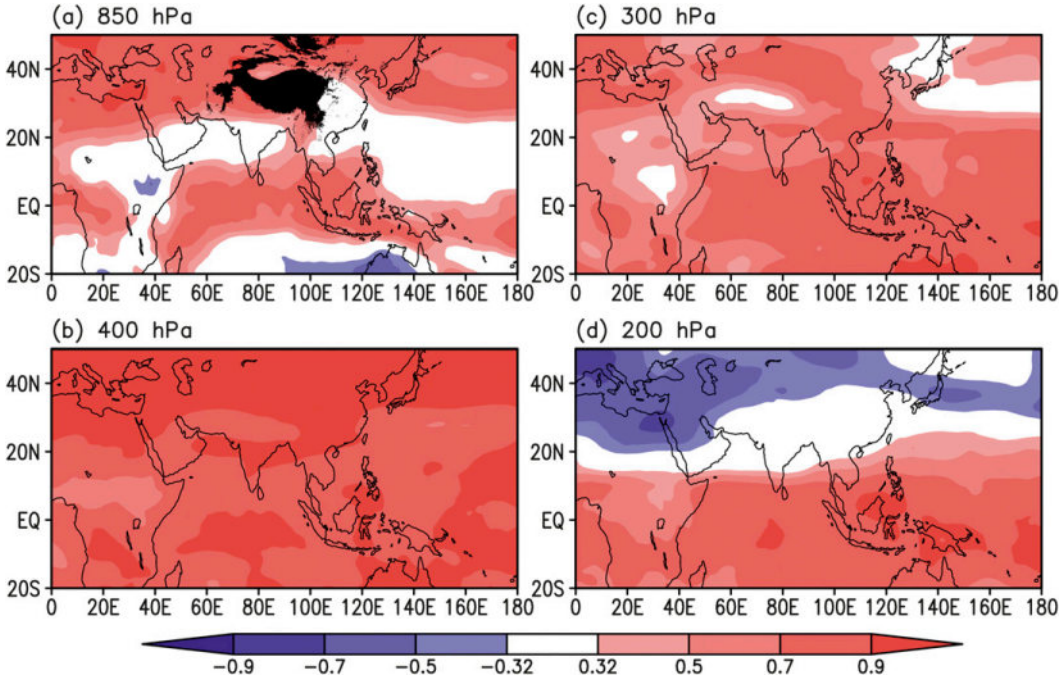

FIG. 1. Patterns of correlation between DJF 500-hPa air temperature and DJF air temperatures at different pressure levels. The black shading denotes the topography.

measured by the area-averaged 500-hPa geopotential height over 30°–45°N, 125°–145°E (Sun and Li 1997), and Niño-3.4 is the averaged SST anomalies over 5°S–5°N, 170°–120°W.

The NCEP CFSv2, whose hindcast is applied in this study, is a fully coupled dynamical prediction system (Saha et al. 2012, manuscript submitted to *J. Climate*). It consists of the NCEP Global Forecast System at T126 spectral resolution, the Geophysical Fluid Dynamics Laboratory Modular Ocean Model version 4.0 at 0.25°–0.5° grids coupled with a two-layer sea ice model, and the four-layer Noah land surface model. Output from the CFSv2 9-month hindcast of 28 years from 1983–2010 is analyzed. Beginning on 1 January, 9-month hindcast runs are initiated from every fifth day and run from all four cycles of that day. An ensemble average of the monthly-mean values of 24 members is used as the prediction, with the initial dates after the seventh of the particular month are used to construct the ensemble prediction for the subsequent month. The winter of a specific year refers to the December of the previous year and the January and February of the current year (DJF). For DJF 0-month lead forecast, it is an ensemble mean of the runs initiated from 2 and 7 December and 12, 17, 22, and 27 November. The longest 7-month lead forecast for DJF is an ensemble mean of the runs initiated from 1 and 6 May and 11, 16, 21, and 26 April.

All statistical significance tests for linear correlation analysis are performed using the two-tailed Student's *t* test. The degrees of freedom are 26 for a time series of 28 samples (1983–2010). The coefficients of correlation at the 90%, 95%, 99%, and 99.9% confidence levels are 0.32, 0.37, 0.48, and 0.59, respectively.

3. Dominant modes of interannual variability of winter UTT over Asia

Previous studies have used the vertically integrated temperature from the lower troposphere to the upper troposphere to measure the TT (Li and Yanai 1996; Liu and Yanai 2001; Gao and Yang 2009; Sun and Yang 2012). Here, we first assess to what extent the air temperatures at various pressure levels vary in phase and then determine the levels on which air temperatures are used to represent the variation of TT.

Figure 1 shows the DJF correlation between 500-hPa air temperature and the temperatures at different levels. Because the mean elevation of TP is more than 4000 m, we first use 500-hPa air temperature as a reference. The variations of TTs at various levels are in phase in most regions (Fig. 1). However, the 500-hPa air temperature does not vary in phase with the temperatures in the lower troposphere over the subtropics and at the levels higher than 200 hPa over the extratropics (Figs. 1a,d), while the temperatures from 500 to 300 hPa vary synchronously. A

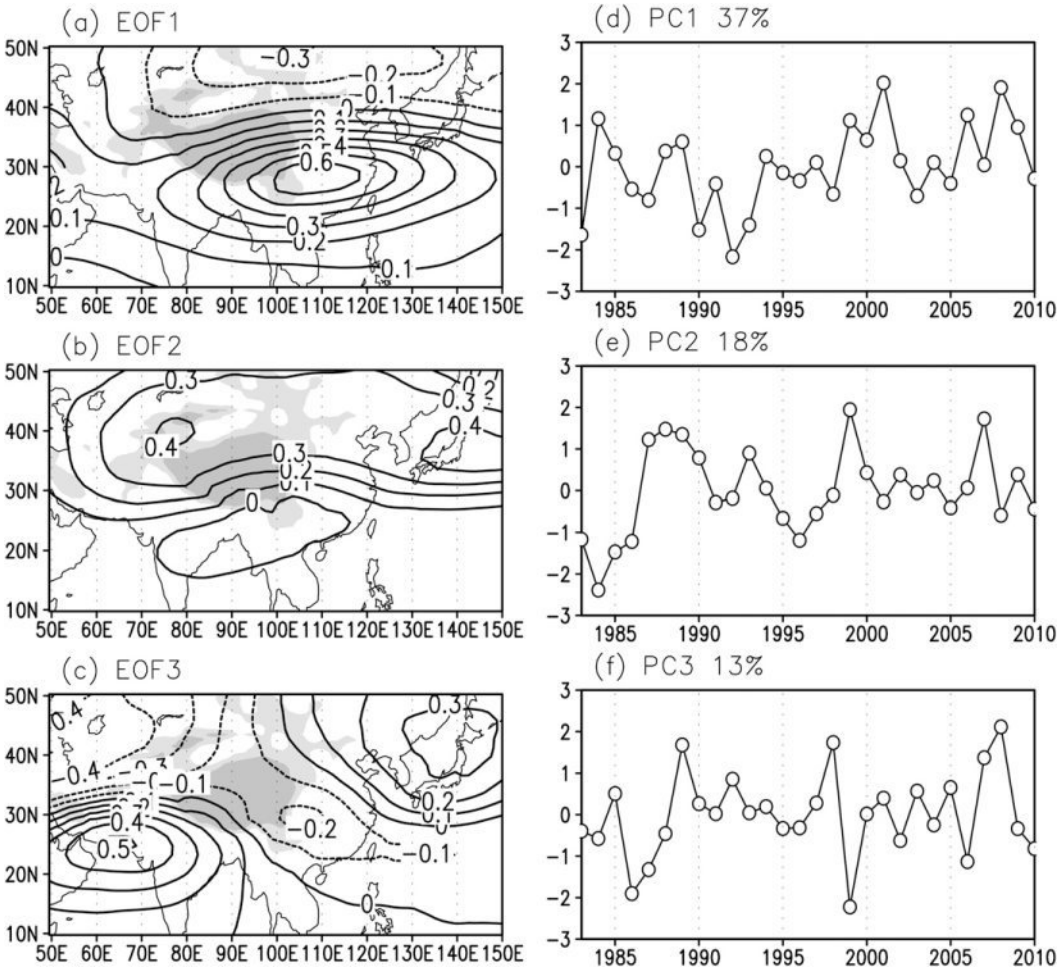

FIG. 2. (a) Spatial pattern and (d) PC of the first mode of an EOF analysis applied to the temporal covariance matrix of DJF vertically integrated temperature from 500 to 300 hPa over 10°–50°N, 50°–150°E. (b),(e) As in (a),(d), but for the second mode. (c),(f) As in (a),(d), but for the third mode. The light (dark) shadings denote the topographic altitude above 1500 (3000) m.

similar feature can also be found when air temperature at other levels is used as the reference. By considering that the mean elevation of the TP is more than 4000 m, we investigate UTT, vertically integrated temperature from 500 to 300 hPa, over Asia in this study.

Figure 2 shows the first three leading modes and corresponding principal components (PCs) of an empirical orthogonal function (EOF) analysis of the temporal covariance matrix of DJF UTT over Asia. They account for 37%, 18%, and 13% of the total variance, respectively, with a sum of 68%. According to the rule given by North et al. (1982), the first and second modes are statistically distinguished from each other, while the second and third modes cannot be solved (not shown). As will be shown later in this paper, however, the first three modes are associated with different physical processes and linked to totally different surface climate variations. The first mode (EOF1) is positive south of 40°N and negative north of 40°N, with a maximum over southern China (Fig. 2a). The second mode is positive with a maximum located to the north of 30°N, with small negative values over part of South Asia (Fig. 2b). The third mode shows a more complicated pattern, with two positive centers over Pakistan and the Sea of Japan and a negative center over central Asia, as well as a small negative band from the eastern TP to the Philippine Sea (Fig. 2c). The first three PCs show large interannual variation (Figs. 2d–f). It should be pointed out that the EOF patterns apparently do not change when the domain of analysis is enlarged (e.g., 10°–50°N, 35°–165°E). Zhao et al. (2008) documented a teleconnection pattern in winter upper-tropospheric temperature with a positive center over Asia and a negative center over the North Pacific. When the domain of EOF analysis is

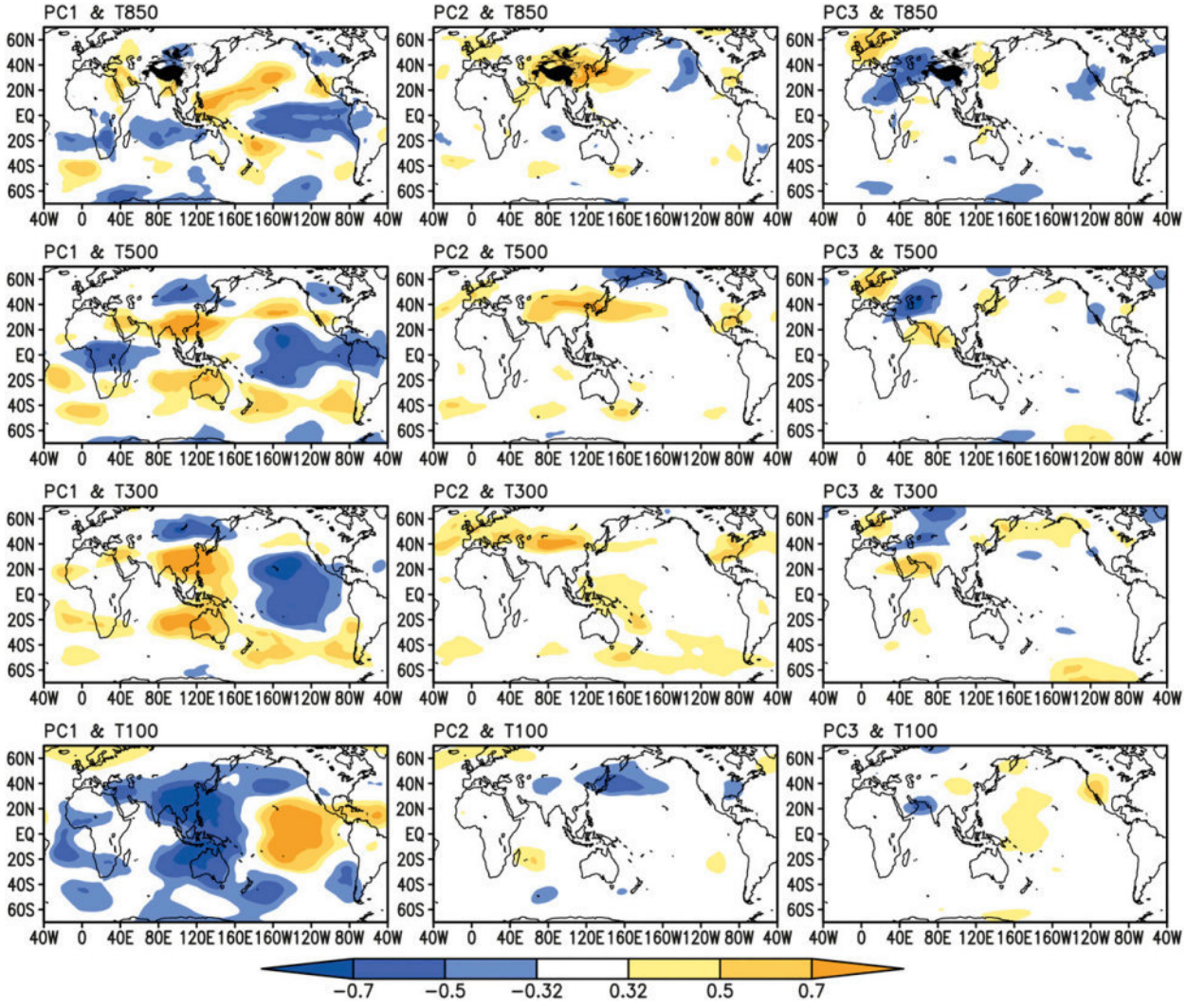

FIG. 3. (top)-(bottom) Patterns of correlation between PCs of EOF analysis and air temperatures at different pressure levels, for (left) the first mode (PC1), (center) the second mode (PC2), and (right) the third mode (PC3). The black shading denotes the topography.

expanded to the entire Northern Hemisphere, the teleconnection pattern is not found. However, this pattern can be found when the EOF analysis is applied to UTT with the zonal mean removed (Zhao et al. 2008). This feature implies that the zonal mean UTT also has strong interannual variations.

As shown in Fig. 1, the UTT is partly coupled with the near-surface temperature. To show the three-dimensional structure of the temperatures associated with the first three leading modes, the correlation between the PCs and the air temperatures at different levels is computed (see Fig. 3). The pattern of correlation between 850-hPa temperature and the first PC (PC1) over oceans is similar to the SST pattern related to La Niña. The patterns of correlation between the PC1 and temperatures at 500 and 300 hPa are symmetrical about the equator, with strong negative correlation from the central Pacific to tropical Africa and from the Lake Balkhash to the Sea of Okhotsk, and strong positive correlation over southeastern Asia and to the northwest of Australia. The correlation between PC1 and 300-hPa temperature is higher than that between PC1 and 500-hPa temperature. The correlation pattern between PC1 and 300-hPa temperature is contrary to that between PC1 and 100-hPa temperature. The temperature anomalies associated with PC1 are similar to those related to ENSO (Trenberth and Smith 2009). Indeed, PC1 is highly correlated with DJF Niño-3.4, with a correlation coefficient of −0.69.

The second PC (PC2) is significantly correlated with the temperatures of 850–300 hPa from Europe to the western North Pacific, even over southeastern North America. This band of significant correlation cannot be

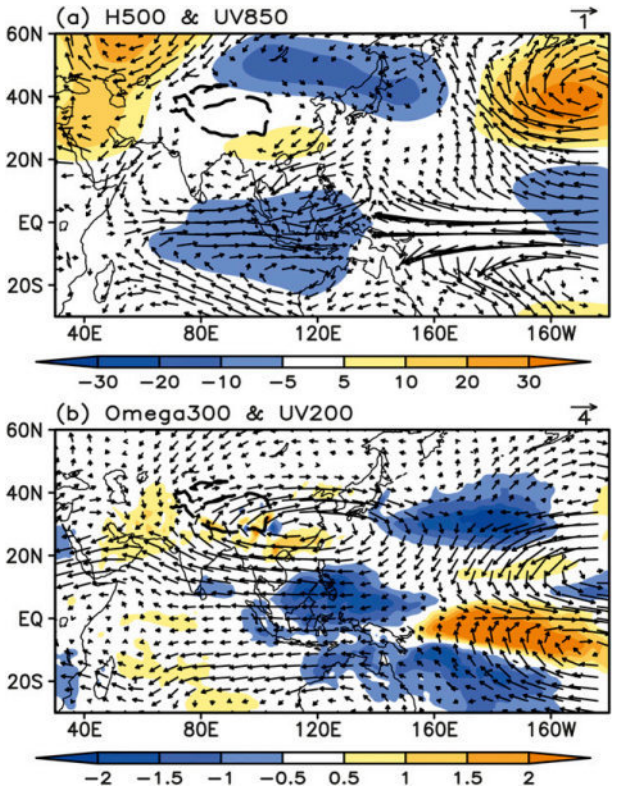

FIG. 4. (a) Patterns of regression of 850-hPa winds ($m\,s^{-1}$; vectors) against PC1 and regression of 500-hPa geopotential height (gpm; shaded) against PC1. (b) Patterns of regression of 200-hPa winds ($m\,s^{-1}$; vectors) against PC1 and regression of 300-hPa vertical pressure velocity ($10^2\,Pa\,s^{-1}$; shaded) against PC1. The long and thick dashed lines denote topographic height of 3000 m.

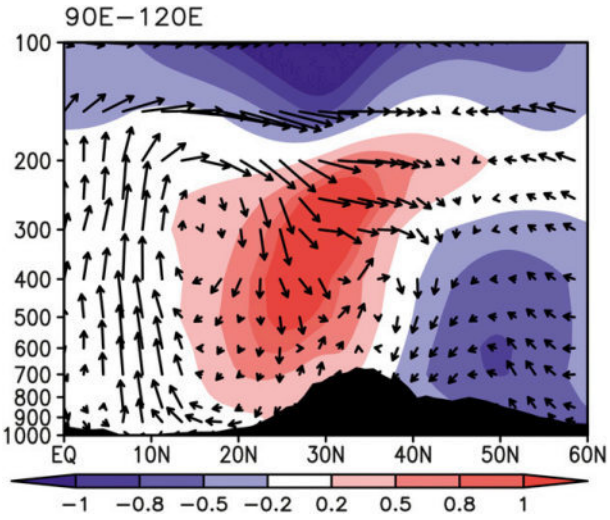

FIG. 5. Latitude–height cross section of averaged (90°–120°E) regression of air temperature (K; shaded) against PC1 and regression of meridional circulation (vectors) against PC1. The black shading denotes the average (90°–120°E) topography.

seen at 100 hPa. The patterns of correlation between the third PC (PC3) and the temperatures at different levels are similar, characterized by strong wave features, with positive centers over northern Europe, the northern Arabian Sea, and the vicinity of Japan and a negative center over the Middle East. These features are more evident for 500 hPa. Thus, the above analyses indicate that the first three modes of winter UTT variations are not regional, but rather large-scale and even planetary-scale phenomena.

4. Atmospheric circulations associated with the leading modes of UTT variations

a. The most dominant mode

Figure 4 shows the regressions of 850-hPa winds, 500-hPa geopotential height, 200-hPa winds, and 300-hPa vertical pressure velocity against PC1, respectively. Because of the high correlation between PC1 and Niño-3.4, the circulation patterns associated with PC1 are similar to those related to ENSO at both the lower troposphere and the upper troposphere. Strong cyclonic circulation appears over the South China Sea and the western Philippine Sea, accompanied by strong ascent motion. The 500-hPa geopotential height is low from the Lake of Baikal to the southern Sea of Okhotsk, accompanied by 850-hPa northerly anomalies over East Asia. Corresponding to the warming to the southeast of TP, there is a strong upper-level anticyclone over East Asia, with descent motion to its western portion. The westerly flow associated with the anticyclone strengthens the EAJS. All circulation anomalies over East Asia indicate a strong East Asian winter monsoon.

Figure 5 presents the latitude–height cross section of 90°–120°E averaged regressions of air temperature and meridional circulation against PC1, respectively. The temperature anomalies over southern China maximize at the upper troposphere, accompanied by a strong sinking motion that is linked to the rising motion around 10°N. Thus, the warming over southern China is contributed by adiabatic heating caused by the sinking motion that is linked to the rising motion over the South China Sea and the western Philippine Sea. Differently, the cooling to the north of 40°N is uniform from the surface to 300 hPa, with anomalous northerlies and rising motion to the north of 50°N.

b. The second mode

Figure 6 shows the regressions of SLP, 850-hPa winds, 500-hPa geopotential height, and 200-hPa winds against PC2, respectively. Associated with PC2, SLP strongly

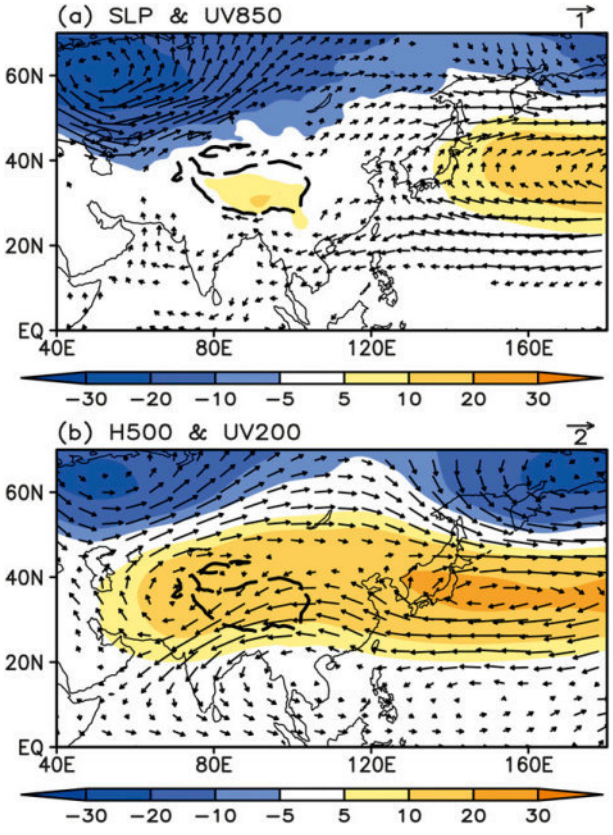

FIG. 6. (a) Patterns of regression of 850-hPa winds ($m\,s^{-1}$; vectors) against PC2 and regression of SLP (10^1 Pa; shaded) against PC2. (b) Patterns of regression of 200-hPa winds ($m\,s^{-1}$; vectors) against PC2 and regression of 500-hPa geopotential height (gpm; shaded) against PC2. The long and thick dashed lines denote topographic height of 3000 m.

decreases over the Ural Mountains and increases over the northwestern North Pacific, accompanied by a cyclonic circulation and an anticyclonic circulation at the lower troposphere, respectively. There is also a decrease in SLP over Siberia. Corresponding to the zonal band of increase in mean UTT, 500-hPa geopotential height increases from the western TP to the northwestern North Pacific, a feature extending to 200 hPa, with anomalous easterlies over 20°–30°E and anomalous westerlies to the north of 40°N. The anomalies associated with PC2 are limited to the mid- and high latitudes and are latitudinally oriented. This feature is similar to that associated with the AO (Jiang et al. 2013b), and the coefficient of correlation between the AO and PC2 is 0.39. Then, is the second mode discussed above a regional characteristic of the AO?

Figure 7 shows the SLP features associated with PC2 and the AO, as well as the correlations between surface air temperature (SAT) and PC2, and between SAT and the AO. The SLP in the Northern Hemisphere associated with PC2 varies out of phase between the north and the south of about 50°N, which is similar to that related to the AO. However, the magnitude and centers of anomalous SLP are different. The anomalous SLP associated with the AO is larger. The strong positive anomalous center related to the AO over the Atlantic is insignificant in the PC2-related SLP, while the anomalous SLP associated with the AO and PC2 over the North Pacific has the same magnitude. Over Asia, the PC2-related SLP gradient is more meridionally oriented compared to the AO-related SLP gradient. As a result, the AO has a significant relationship with the SAT mostly to the north of 50°N, while the PC2 is significantly correlated with the SAT to the south of 50°N. Moreover, the SAT significantly correlated with PC2 can extend southward to the tropics, associated with a large meridional SLP gradient between East Asia and oceans. In addition, the correlation between PC2 and SAT is insignificant over most of the Atlantic, Europe, and North Africa. Thus, the second mode is not a regional feature of the AO, but is partially associated with the AO.

c. *The third mode*

Figure 8 shows the regressions of SLP, 700-hPa winds, 500-hPa geopotential height, and 200-hPa winds against PC3, respectively. The circulation associated with PC3 features a wavelike pattern. The SLP is negative to the north of 50°N, while large positive anomalies are centered over the Mediterranean Sea and northeast Asia. The two positive anomalous centers are more obvious at 500-hPa geopotential height, accompanied by two strong negative anomalous centers over Greenland and the Ural Mountains. The wavelike pattern is well recognized from the anomalous 200-hPa winds, with two wave trains. The wave trains have two same centers, with a cyclonic circulation over Greenland and an anticyclonic circulation over the Mediterranean Sea. The northern branch is associated with a cyclonic circulation over the Ural Mountains and an anticyclonic circulation over the Sea of Japan, while the southern branch is associated with cyclonic circulations over the Middle East and southeast of the TP and anticyclonic circulations over the Arabian Sea and the Sea of Japan. The northern branch may be formed by stationary waves propagating along the subpolar waveguide (Sun and Yang 2012), and the southern branch by quasi-stationary Rossby waves trapped on the Asian jet stream (Watanabe 2004). The intensification of the MEJS is also noted in Fig. 8b, which has a quasi-barotropic structure, accompanied by large westerly anomalies at the lower troposphere (Fig. 8a). Because of the mechanical obstruction of the TP, the strong anomalous westerlies lead to an anomalous cyclonic circulation to the southeast of TP, which often causes severe climate anomalies over China (Wen et al. 2009).

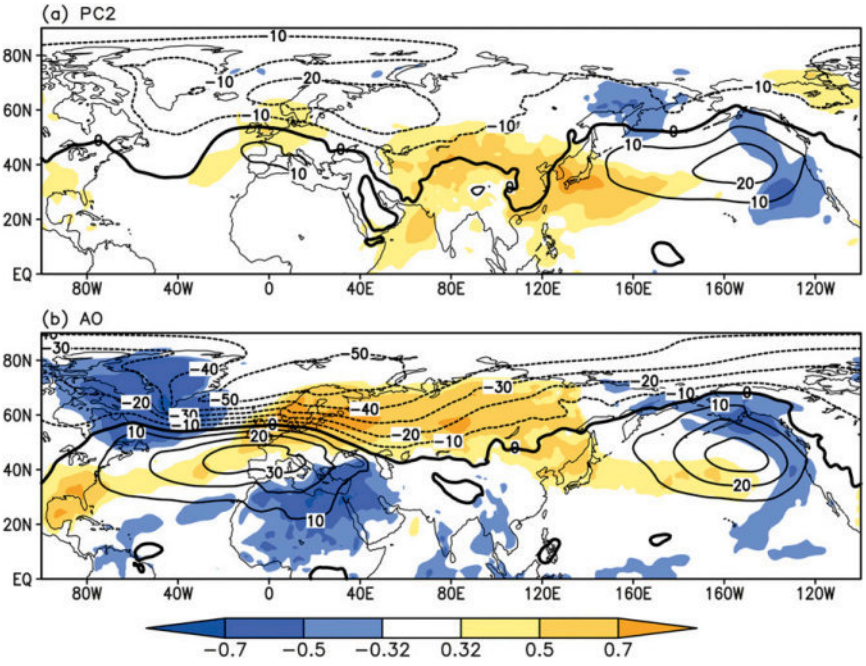

FIG. 7. (a) Patterns of regression of SLP (10^1 Pa; contours) against PC2 and correlation between SAT and PC2. (b) As in (a), but PC2 is replaced by the AO index.

Variations of the MEJS are also an important signal for the following Asian summer monsoon (Yang et al. 2004). The MEJS is highly correlated with PC3, with a correlation coefficient of 0.55. The patterns of SLP, 700-hPa winds, 500-hPa geopotential height, and 200-hPa winds associated with the MEJS are shown in Fig. 9. The MEJS-related patterns are similar to those associated with PC3, except with a closer link to tropical circulation and a weaker link to the circulation over Greenland. From this perspective, the anomalies over Greenland may be not the origins of the two wave trains. Instead, the anomalies over the Mediterranean Sea may be important for the wave trains, at least for the southern one (Watanabe 2004). In addition, although both the AO and the NAO are associated with strong anomalies over the North Atlantic [Fig. 7b; the NAO pattern is available at http://www.cpc.ncep.noaa.gov/products/precip/CWlink/pna/nao_loading.html or see Li and Wang (2003b)], the PC3 is just significantly correlated with the AO, with a correlation coefficient of 0.38, since the AO is associated with the strong anomalies over the Mediterranean Sea.

5. Surface climate associated with the dominant modes

Analysis in the previous section indicates that the first three modes of winter UTT variations over Asia are linked to large-scale circulation anomalies. Here, we further investigate the surface climate anomalies that are related to these modes.

Figure 10 displays the patterns of correlation between SAT and the first three PCs. As discussed before, the PC1 is significantly correlated with Niño-3.4. Thus, the PC1-related SAT anomalies concentrate mostly over oceans, similar to the pattern of SST related to ENSO. Over land, significant correlations are found over the Middle East, the southeastern TP, and part of North America (Fig. 10a). Because of the anomalous temperature center of the first mode at the upper troposphere (Fig. 5), the PC1 is just correlated with SAT at the southeastern TP, rather than to the east of TP. As for PC2, it is significantly correlated with the SAT over most of Asia. Thus, the variation of the second mode is important for prediction of the Asian SAT. The PC3 shows significant correlations with the SAT over northern Europe, the Middle East, eastern North Africa, and Japan.

Patterns of correlation between precipitation and the first three PCs are shown in Fig. 11. As expected, the PC1 is associated with excessive precipitation over the Maritime Continent, corresponding to the lower-tropospheric cyclonic circulation and the strong rising motion in the troposphere (Figs. 4a, 5, and 11a), while deficient precipitation is found from equatorial eastern Africa to the southwest of the TP and over southern China and the

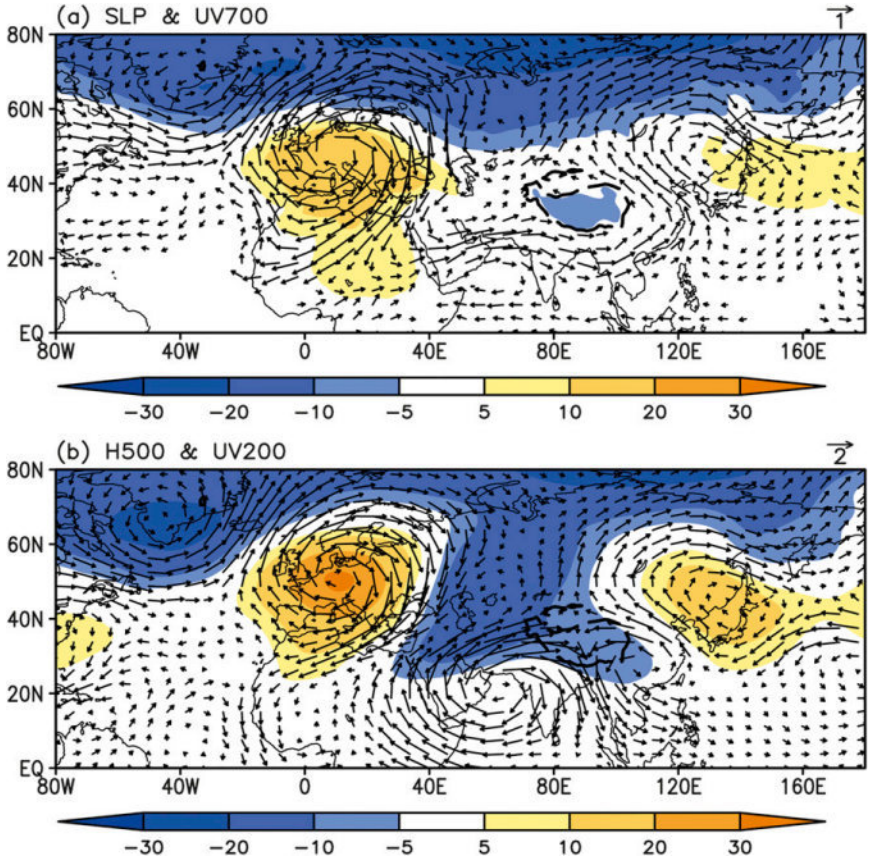

FIG. 8. (a) Patterns of regression of 700-hPa winds ($m\,s^{-1}$; vectors) against PC3 and regression of SLP (10^1 Pa; shaded) against PC3. (b) Patterns of regression of 200-hPa winds ($m\,s^{-1}$; vectors) against PC3 and regression of 500-hPa geopotential height (gpm; shaded) against PC3. The long and thick dashed lines denote topographic height of 3000 m.

Korean Peninsula. Although PC2 is significantly correlated with the SAT over Asia, it shows no strong relationship with the precipitation over the region. Different from the first two modes, the PC3 is positively and significantly correlated with the precipitation from the eastern TP to the south of Japan, and over the equatorial eastern Indian Ocean. The excessive precipitation associated with PC3 is likely caused by the lower-tropospheric cyclonic circulation to the southeast of TP, which transports substantial water vapor northward.

The precipitation and SAT applied in the above analyses are from reanalysis products. To verify the significant correlation between the first three PCs and surface climate, we recalculate the correlation using station precipitation and SAT from China. As shown in Fig. 12, the correlation patterns over China are the same as those in Figs. 10 and 11. Even the pattern of correlation between PC1 and SAT over the TP, where analysis data may have large biases, is similar to the pattern calculated from the SAT from the ERA-Interim reanalysis. The first mode is associated with the precipitation anomalies over southern China, ascribed to the dominance of ENSO (e.g., Wu et al. 2003; Zhou et al. 2010; Jiang et al. 2013b). The PC3 is significantly correlated with the precipitation over the middle and lower reaches of the Yangtze River basin and the northeastern flank of the TP.

The above analyses indicate that the first three modes are significantly correlated with the surface climate anomalies over East Asia. This feature is attributed to the high correlations between the PCs and the major circulations that affect East Asian climate (Table 1). PC1 is highly correlated with ENSO but less correlated with the AO or the NAO. There are significant correlations between PC1 and the SH, the MEJS, and the EAJS, respectively. Although the features associated with PC1 show a strong East Asian winter monsoon, there is no significant decrease in SAT over East Asia. Wang et al. (2010) reported that the East Asian winter

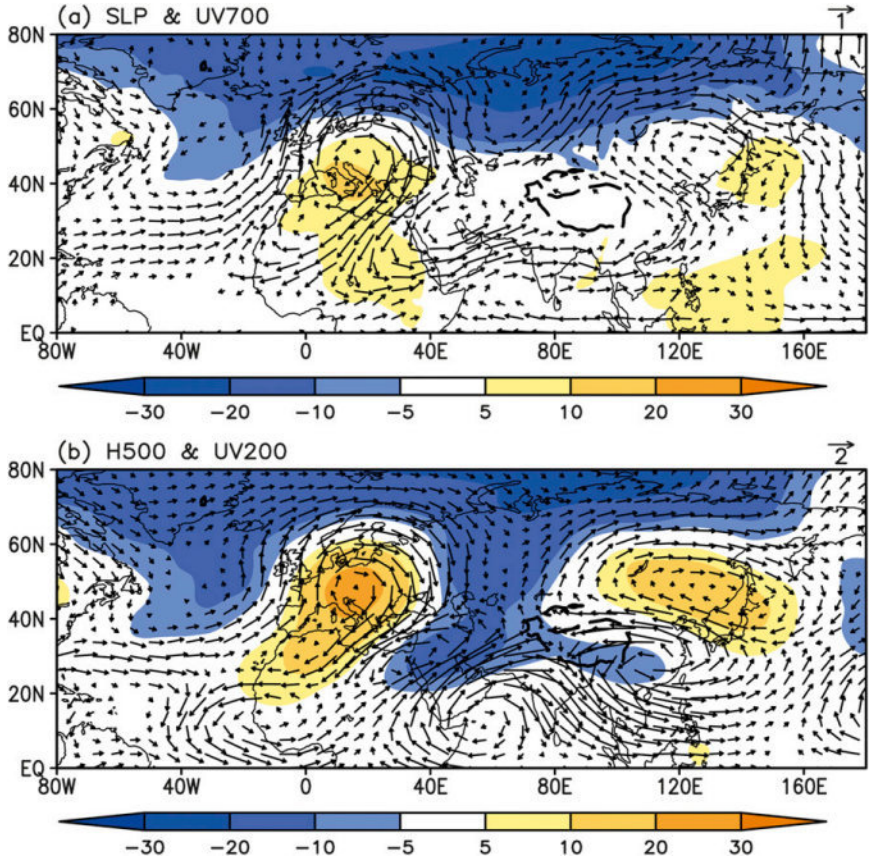

FIG. 9. As in Fig. 8, but PC3 is replaced by the MEJS index.

monsoon has two distinct modes. The southern mode features a deepening EAT and increased surface pressure over Mongolia, representing a cold winter south of 40°N. The EAT is an element that governs the path and strength of cold air affecting East Asia. A deepened EAT favors a cold winter to the south of 40°N. However, PC1 is not significantly correlated with EAT, whereas it is significantly correlated with SH and EAJS. On the other hand, the PC2 is highly correlated with the EAT, and so is the SAT over East Asia. Thus, the weak relationship between the first mode and the EAT is one of the reasons why the mode is not associated with the anomaly of SAT over East Asia to a significant degree. Both PC2 and PC3 are significantly correlated with AO, indicating that the AO may affect the East Asian winter climate in different ways.

To further illustrate that the surface climate anomalies over East Asia are linked to the first three UTT modes, we analyze the composite patterns of circulations and surface climate anomalies of some specific years. We select the years with the anomalies of normalized PCs exceeding one standard deviation to conduct the composite analysis. Table 2 lists the selected years for the three leading modes based on this criterion. It is seen that all the five positive years of PC1 are La Niña years, while only half of the negative years are El Niño years, according to the ENSO criterion of the Climate Prediction Center (available at http://www.cpc.ncep.noaa.gov/products/analysis_monitoring/ensostuff/ensoyears.shtml). This feature highlights the strong link of the first mode to ENSO.

Figure 13 shows the composite patterns of difference in UTT, precipitation, temperature, and 500-hPa geopotential height between positive years and negative years of PC1. The pattern of UTT is similar to the spatial pattern of EOF1, with significant warming in the middle and upper troposphere over southern China (Fig. 13a). There is a significant decrease in precipitation over southern China, with a center to the south of 25°N and over the Korean Peninsula (Fig. 13b). Temperature increases significantly over southeastern TP and northwestern Indo-China peninsula, with a maximum temperature difference about 2°C, whereas it decreases to the north of 35°N, with significant anomalies over northern Japan (Fig. 13c). The first mode is associated with a significant increase in 500-hPa geopotential height over

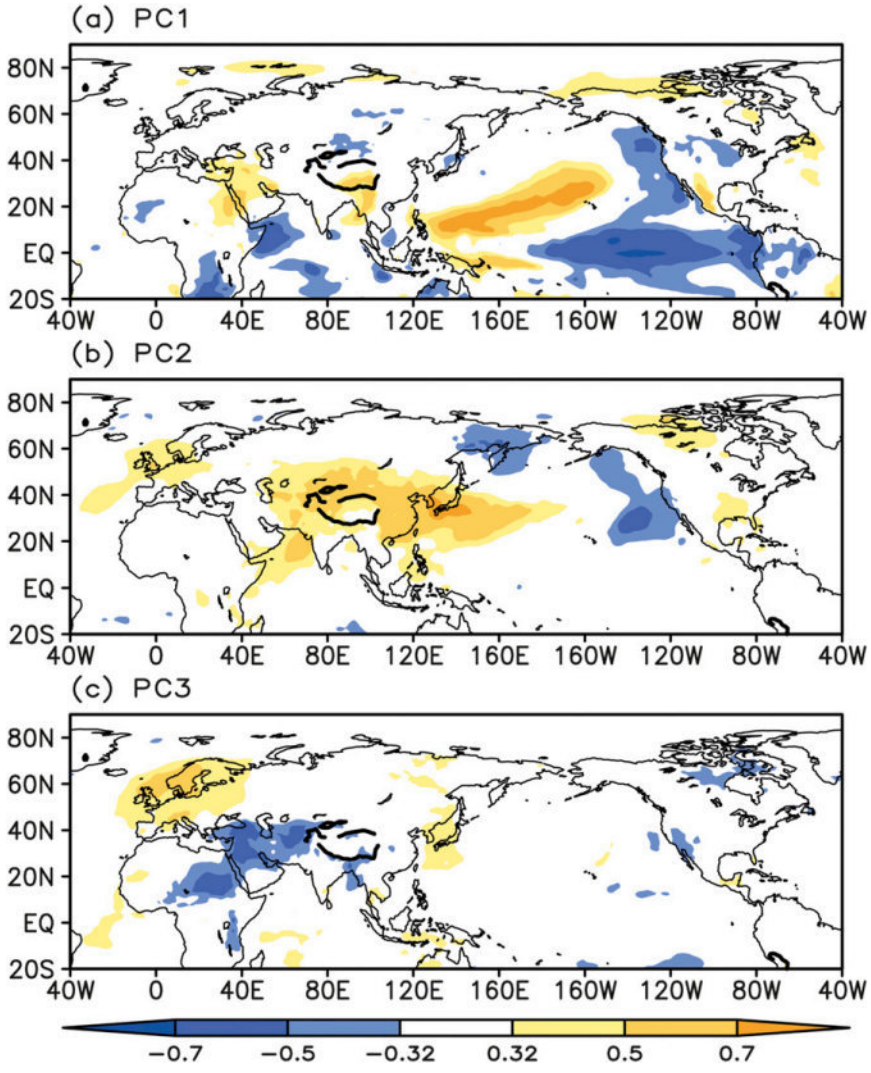

FIG. 10. Patterns of correlation between SAT and (a) PC1, (b) PC2, and (c) PC3. The long and thick dashed lines denote topographic height of 3000 m.

southern China, indicating a westward shift of the western North Pacific high, which is unfavorable for decreases in SAT over southern China (Fig. 13d).

Figure 14 exhibits the composite patterns of difference in UTT, temperature, 500-hPa geopotential height, and 925-hPa winds between positive years and negative years of PC2. The pattern of UTT is also similar to the spatial pattern of the second mode, with significant UTT anomalies from western TP to the east of Japan (Fig. 14a). The second mode is associated with a significant increase in SAT over East Asia, with a difference exceeding 2°C over most East Asia (Fig. 14b). The second mode is associated with a significant increase in 500-hPa geopotential height over Asia, with a center over northeastern Asia, indicating a very shallow EAT (Fig. 14c). The 500-hPa geopotential height anomaly also indicates a strong subtropical high. The second mode is accompanied by significant southerly anomalies (Fig. 14d). All the circulation anomalies favor a warm winter over East Asia.

Figure 15 shows the composite patterns of difference in UTT, precipitation, 500-hPa geopotential height, and 700-hPa winds between positive years and negative years of PC3. The composite UTT for the third mode shows three significant anomalous centers, with positive centers over the northern Arabian Sea and northern Japan and a negative center over central Asia (Fig. 15a). The precipitation associated with third mode significantly increases over southern China and to the south of Japan (Fig. 15b). Because northern China receives less

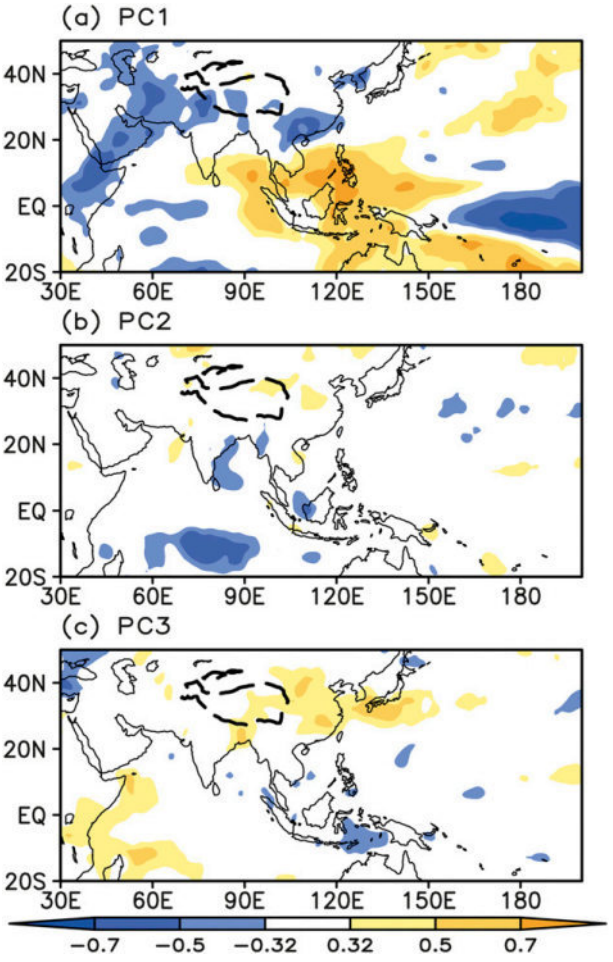

FIG. 11. As in Fig. 10, but SAT is replaced by precipitation.

precipitation during winter, the composite precipitation is very small to the northeast of TP, where correlation between precipitation and PC3 is significant. The anomalous precipitation center over southern China is located northward compared to that related to the first mode. The 500-hPa geopotential height decreases significantly from central Asia to southeastern TP, accompanied by the anomalous cyclonic circulation along the southern and eastern edges of TP. This anomalous cyclonic circulation and the anomalous anticyclonic circulation over northeast Asia form a latitudinally oriented trough over southern China and a lower-tropospheric convergence zone to the south of Japan, which receives above normal precipitation (Figs. 15b,d).

6. Prediction of the dominant modes by CFSv2

As shown above, the first three modes of winter UTT over Asia are accompanied by significant surface climate anomalies over East Asia and are linked to anomalies of large-scale circulation patterns. How can these dominant modes be predicted by state-of-the-art climate models? Here, we try to answer this question by analyzing the hindcast of NCEP CFSv2. Because of the unavailability of 400-hPa temperature in the hindcast, we use the mean of the 500- and 300-hPa temperatures to represent the CFS UTT over Asia. Nevertheless, the variability of the mean temperature of 500 and 300 hPa is similar to that of the vertically integrated temperature from 500 to 300 hPa in observations. The tropospheric temperature of the CFSv2 hindcast has a strong shift around 1998 resulting from the ingestion of the Advanced Television Infrared Observation Satellite (TIROS) Operational Vertical Sounder (ATOVS) data in the NCEP Climate Forecast System Reanalysis (Zhang et al. 2012), used as the initial condition for CFSv2 hindcast. Thus, the departures of UTT are calculated for two different periods, 1983–98 and 1999–2010.

Figure 16 shows the first three modes of an EOF analysis of temporal covariance matrix of DJF UTT from the CFSv2 0-month-lead hindcast. The spatial pattern and principal component of the first two EOF modes are well predicted, with the coefficients of pattern correlation between observation and 0-month prediction being 0.90 and 0.81 for EOF1 and EOF2, respectively, although the predicted spatial pattern of the second mode has an unrealistic negative center to the southeast of the TP. The PCs of the first two EOF modes are also well predicted, with the coefficients of temporal correlation between observation and 0-month prediction being 0.64 and 0.53 for PC1 and PC2, respectively. Although the predicted PC3 is significantly correlated with observation, with a correlation coefficient of 0.44, the hindcast fails to capture the observed spatial pattern of the third mode. The variances explained by the first two modes are higher than those for observations.

Although the first two modes are well captured by 0-month lead hindcast, only the first mode can be predicted in long leads. The coefficients of pattern correlation between predicted EOF1s and observation are above 0.75 for all time leads, with an overall decrease with lead time (Fig. 17). The skill of CFSv2 for PC1 shows a decrease from 0-month lead to 2-month lead, and a slight increase afterward. The high predictability of the first mode is attributed to the high skill of CFSv2 in predicting ENSO and related teleconnection patterns (Jiang et al. 2013b). Thus, the lowest skill in predicting PC1 by 2 months in advance may be owing to the spring predictability barrier of ENSO. Why does the CFSv2 show a slight increase in prediction skill of the first mode? This feature may be partially because that the variance explained by the first mode has an increasing trend as lead time increases (Table 3), implying that the

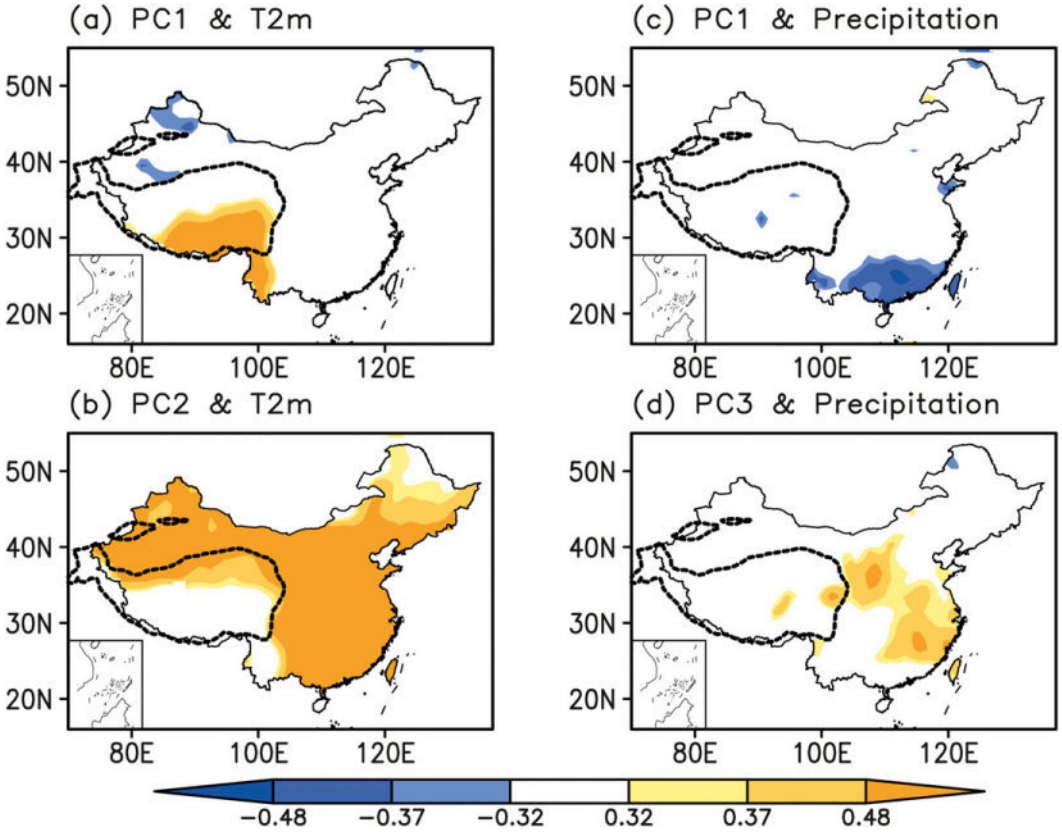

FIG. 12. Patterns of correlation between observed SAT in China and (a) PC1 and (b) PC2. (c),(d) As in (a),(b), but SAT is replaced by precipitation and PC2 in (b) is replaced by PC3 in (d). The long and thick dashed lines denote topographic height of 3000 m.

interannual variation of UTT over the TP is increasingly dominated by ENSO in the CFSv2 with increase in lead time.

7. Summary and discussion

a. Summary

Previous studies have shown that the variation of TT has a close link to some well-known climate patterns. The severe winter climate anomalies in recent years are associated with apparent TT anomalies over the TP. However, the interannual variation of winter TT over Asia is unclear. In this study, we investigate the dominant modes of winter UTT variations. The first three EOF modes of winter UTT are discussed, focusing on large-scale atmospheric circulation, surface climate, and the predictability of dominant modes.

The three leading modes of the EOF analysis of temporal covariance of winter UTT over Asia account for 68% of the total variance. The first mode shows a dipole structure, with a strong positive center over southern China and a weak negative center over Mongolia. The

TABLE 1. Correlations of PCs with Niño-3.4, the Arctic Oscillation (AO), the North Atlantic Oscillation (NAO), the Siberian high (SH), the East Asian trough (EAT), the Middle East jet stream (MEJS), and the East Asian jet stream (EAJS). Values in italic and bold font exceed the confidence levels of 95% and 99%, respectively.

	Niño-3.4	AO	NAO	SH	EAT	MEJS	EAJS
PC1	**−0.69**	−0.07	0.05	*0.44*	−0.24	**−0.50**	*0.47*
PC2	−0.03	*0.39*	0.18	*−0.45*	**0.75**	−0.07	**−0.48**
PC3	0.07	*0.38*	0.16	−0.21	**0.48**	**0.55**	−0.32

TABLE 2. Years of positive and negative leading modes, selected by the criterion that the anomalies of normalized PCs exceeding one standard deviation.

	Positive	Negative
PC1	1984, 1999, 2001, 2006, and 2008	1983, 1990, 1992, and 1993
PC2	1987–89, 1999, and 2007	1982–85 and 1996
PC3	1989, 1998, 2007, and 2008	1986, 1987, 1999, and 2006

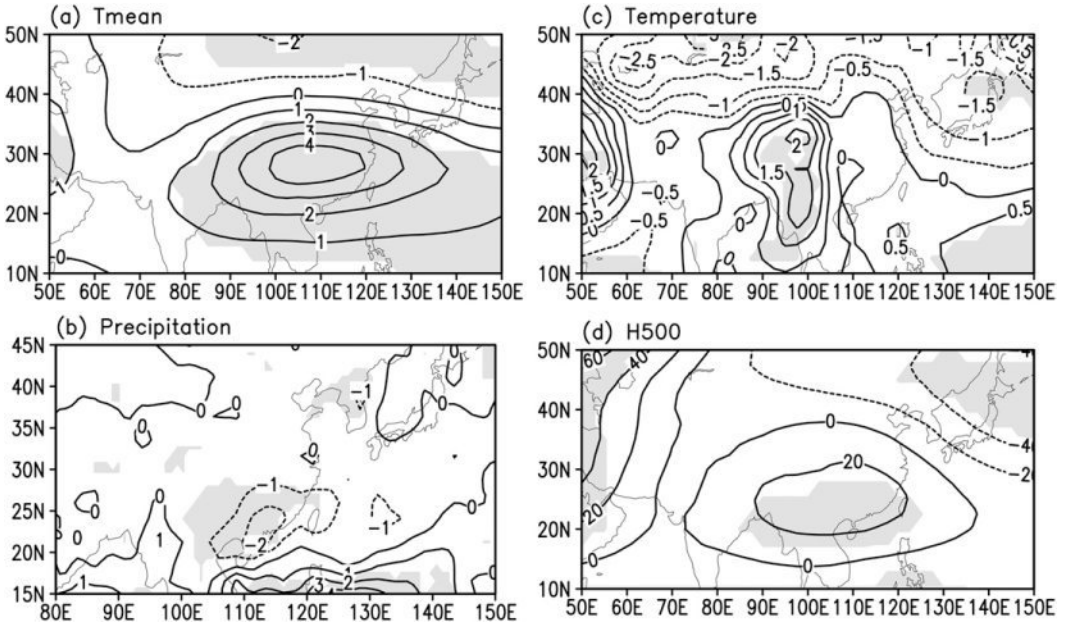

FIG. 13. Composite difference in DJF (a) mean temperature from 500 to 300 hPa (°C), (b) precipitation (mm day^{-1}), (c) SAT (°C), and (d) 500-hPa geopotential height (gpm) between positive years and negative years of the first EOF mode (see Table 2 for details). Values exceeding the 90% confidence level are shaded.

second mode features a monopole variation, with a center from the northwestern TP to the Sea of Japan. The third mode has a tripole pattern, with two positive centers over Pakistan and over the Sea of Japan and a negative center over central Asia.

The first mode is linked to ENSO, and the warming over southern China is contributed by the adiabatic descent induced by the convection to the north of Maritime Continent. The second mode is associated with the AO-like circulation anomalies, but with strong meridional

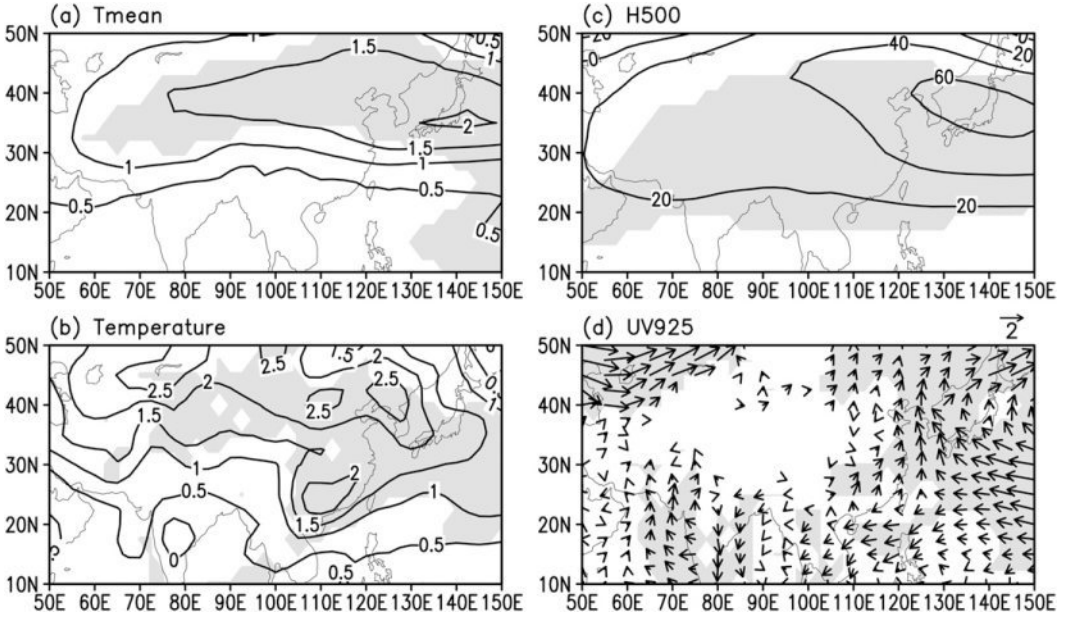

FIG. 14. Composite difference in DJF (a) mean temperature from 500 to 300 hPa (°C), (b) SAT (°C), (c) 500-hPa geopotential height (gpm), and (d) 925-hPa winds (m s^{-1}) between positive years and negative years of the second EOF mode (see Table 2 for details). Values exceeding the 90% confidence level are shaded.

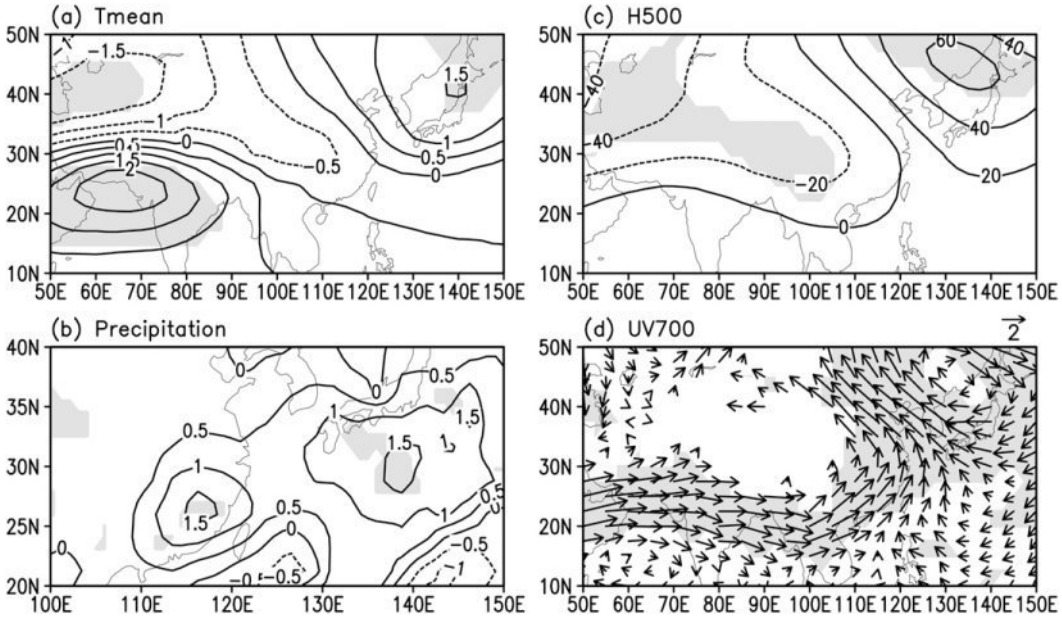

FIG. 15. As in Fig. 14, but for the third EOF mode and (d) is replaced by 700-hPa winds ($m\,s^{-1}$).

gradient of SLP over Asia. The third mode features a wavelike pattern, with two wave trains. The northern branch is from Greenland to the Sea of Japan, formed likely by stationary waves propagating along the subpolar waveguide. The southern branch is from the Mediterranean Sea to the Sea of Japan, formed by quasi-stationary Rossby waves trapped on the Asian jet. The third mode is also associated with variations of the MEJS.

The above dominant modes have close relationships with surface climate both over and beyond East Asia. The first mode is accompanied by warming over the southeastern TP and deficient precipitation over southern China, the Korean Peninsula, and from equatorial eastern Africa to the southwest of TP. The second mode is associated with significant warming over most of Asia, especially East Asia. The third mode is related to excessive precipitation from the eastern TP to south of Japan.

The NCEP CFSv2 has high skill in predicting the first mode but shows little skill in predicting the second and third modes. The high predictability of the first mode is because the CFSv2 has high skill in predicting ENSO and the related teleconnection patterns (Jiang et al. 2013b). The inability of CFSv2 to predict the second and third modes may be ascribed to the unrealistic prediction of AO by the model (Jiang et al. 2013b).

b. Discussion

ENSO-related teleconnection patterns are the basis for seasonal prediction and they can be predicted by dynamical models with reasonable skill. Because of the persistence of ENSO, the pattern of correlation between PC1 and autumn SST resembles an ENSO-related pattern (not shown). Thus, the autumn SST is a precursor of the first mode addressed in this study.

The second and third modes cannot be predicted by CFSv2 in advance even by one month. Is there any precursor of these two modes? The spring thermal condition over the TP has been known as a precursor of Asian summer climate anomalies through the persistence of snow anomalies (Wu and Kirtman 2007; Zhao et al. 2007a; Wu et al. 2010, 2012a,b). Is the autumn thermal anomaly over the TP a precursor of winter climate anomalies? Figures 18a and 18b show correlations of PC2 with autumn 500-hPa geopotential height and temperature, respectively. The PC2 is highly correlated with the autumn 500-hPa geopotential height and temperature over the western TP and correlation is higher for the former than for the latter. Thus, the anomaly of 500-hPa geopotential height over the TP may be a precursor of the second mode. For convenience, we define Hwtp as the mean autumn 500-hPa geopotential height over the western TP (30°–40°N, 70°–90°E). The Hwtp is positively correlated with the winter surface air temperature over most East Asia, with centers over the eastern TP and northern China (Fig. 18c). Because of the westerly flow over the TP, the temperature anomalies over the TP can affect the temperature downstream, as seen in the positive correlation between Hwtp and the UTT from the eastern TP and to northern China (Fig. 18d). How are the anomalies of autumn geopotential

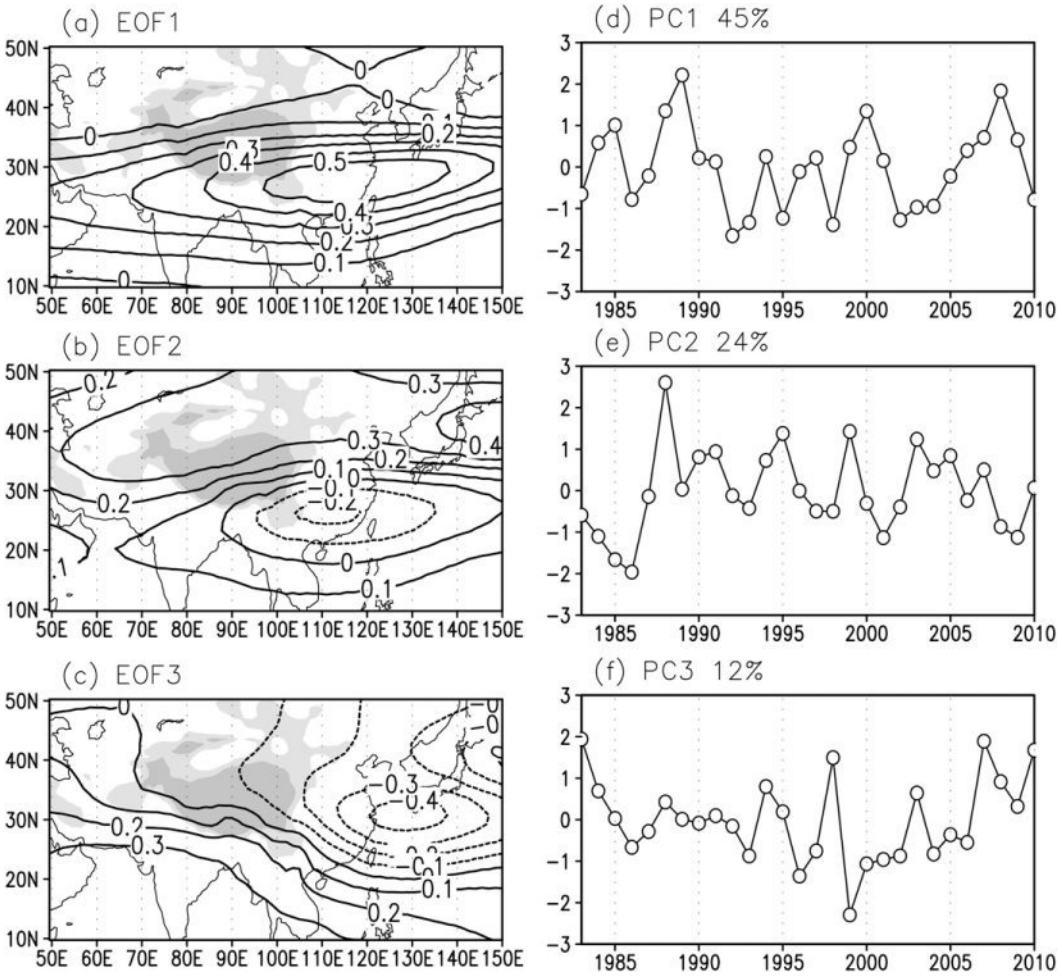

FIG. 16. As in Fig. 2, but for the averaged air temperature of 500 and 300 hPa from CFSv2 ensemble-means of 0-month lead hindcast.

height linked to the winter temperature anomalies over the TP? Yang et al. (2004) discussed that land–atmosphere interaction enhanced the persistency of surface climate features over and to the west of the TP.

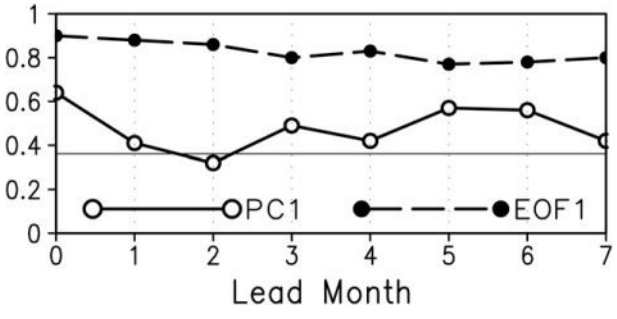

FIG. 17. Solid curves with open circles (long dashed curves with closed circles) denote coefficients of correlation between the EOF analysis PC1 (EOF1) derived from observed temperature and the PC1s (EOF1s) derived from CFSv2 hindcasts of different lead months.

Lin and Wu (2011) reported that the autumn TP snow cover anomalies could persist into the following winter. Thus, the following hypothesis is proposed. An increase in the autumn geopotential height over the western TP leads to a decrease in local snow. The condition of decreased snow persists from autumn to winter, resulting in an increase in winter surface air temperature over the TP. More studies are needed to address the physical and dynamical processes of the hypothesized links. Future investigation of the forcing factors of the two wave trains

TABLE 3. Percentage variances accounted for by various EOF modes for different lead months (LMs).

	LM0	LM1	LM2	LM3	LM4	LM5	LM6	LM7
EOF1	45	47	51	52	59	56	60	53
EOF2	24	24	20	23	19	23	18	22
EOF3	12	13	16	13	9	12	11	12

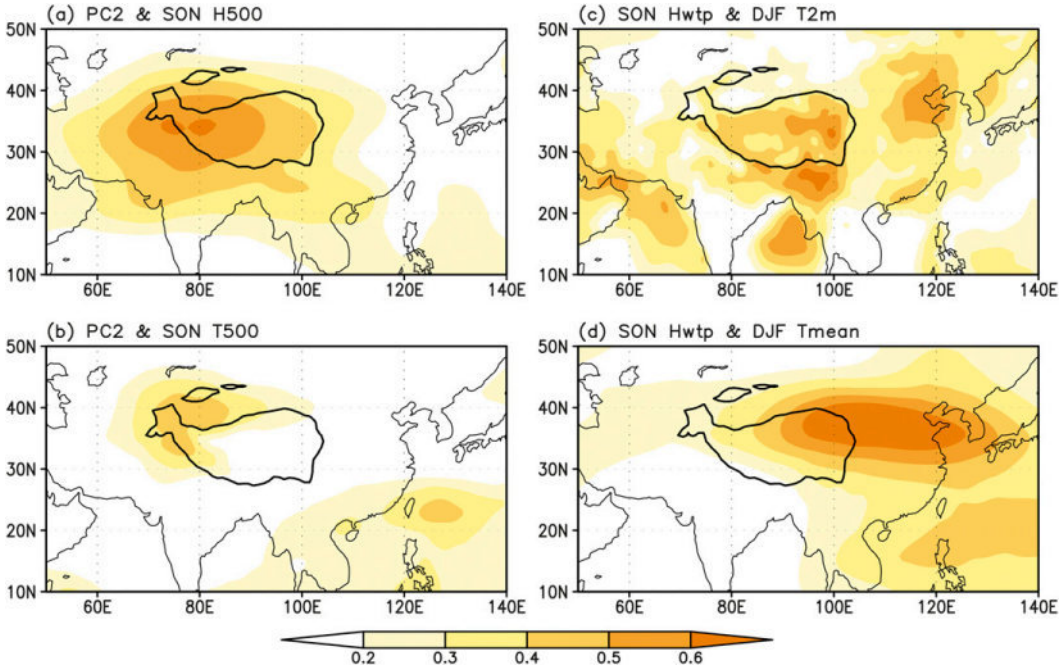

FIG. 18. (a) Pattern of correlation between DJF PC2 and SON 500-hPa geopotential height. (b) Pattern of correlation between DJF PC2 and September–November (SON) 500-hPa air temperature. (c) Pattern of correlation between SON 500-hPa geopotential height over the western Tibetan Plateau (Hwtp; 30°–40°N, 70°–90°E) and DJF surface air temperature. (d) Pattern of correlation between SON Hwtp and DJF vertically integrated temperature from 500 to 300 hPa. The thick black contour denotes topographic height of 3000 m.

associated with the third mode discussed in this study may also be important for enhancing the prediction of winter precipitation over East Asia.

Acknowledgments. This study was jointly supported by the National Basic Research Program of China (Grant 2012CB417202), the National Natural Science Foundation of China (Grant 41105061), the Basic Research and Operation Program of the CMA Institute of Plateau Meteorology (Grant BROP201215, BROP201318), and the Sun Yat-sen University "985 Project" Phase 3. Xingwen Jiang, who was partially supported by the National Oceanic and Atmospheric Administration and the China Meteorological Administration Bilateral Program, thanks NOAA's Climate Prediction Center for hosting his visit while this study was conducted.

REFERENCES

Chang, C. P., 2004: *East Asian Monsoon.* World Scientific, 564 pp.

Chou, C., 2003: Land–sea heating contrast in an idealized Asian summer monsoon. *Climate Dyn.,* **21,** 11–25.

Dee, D. P., and Coauthors, 2011: The ERA-Interim reanalysis: Configuration and performance of the data assimilation system. *Quart. J. Roy. Meteor. Soc.,* **137,** 553–597.

Gao, H., and S. Yang, 2009: A severe drought event in northern China in winter 2008–2009 and the possible influences of La Niña and Tibetan Plateau. *J. Geophys. Res.,* **114,** D24104, doi:10.1029/2009JD012430.

Gong, D. Y., S. W. Wang, and J. H. Zhu, 2001: East Asian winter monsoon and Arctic Oscillation. *Geophys. Res. Lett.,* **28,** 2073–2076.

Jiang, X., Y. Li, S. Yang, and R. Wu, 2011: Interannual and interdecadal variations of the South Asian and western Pacific subtropical highs and their relationships with Asian–Pacific summer climate. *Meteor. Atmos. Phys.,* **113,** 171–180.

——, S. Yang, Y. Li, A. Kumar, X. Liu, Z. Zuo, and B. Jha, 2013a: Seasonal-to-interannual prediction of the Asian summer monsoon in the NCEP Climate Forecast System version 2. *J. Climate,* **26,** 3708–3727.

——, ——, ——, ——, W. Wang, and Z. Gao, 2013b: Dynamical prediction of the East Asian winter monsoon by the NCEP climate forecast system. *J. Geophys. Res.,* **118,** 1312–1328, doi:10.1002/jgrd.50193.

Li, C., and M. Yanai, 1996: The onset and interannual variability of the Asian summer monsoon in relation to land–sea thermal contrast. *J. Climate,* **9,** 358–375.

Li, J., 2005: Coupled air–sea oscillations and climate variations in China. *Climate and Environmental Evolution in China,* Vol. 1, D. Qin, Ed., China Meteorological Press, 324–333.

——, and J. X. L. Wang, 2003a: A modified zonal index and its physical sense. *Geophys. Res. Lett.,* **30,** 1632, doi:10.1029/2003GL017441.

——, and ——, 2003b: A new North Atlantic Oscillation index and its variability. *Adv. Atmos. Sci.,* **20,** 661–676.

Lin, H., and Z. Wu, 2011: Contribution of the autumn Tibetan Plateau snow cover to seasonal prediction of North American winter temperature. *J. Climate,* **24,** 2801–2813.

Liu, X. D., and M. Yanai, 2001: Relationship between the Indian monsoon precipitation and the tropospheric temperature over the Eurasian continent. *Quart. J. Roy. Meteor. Soc.,* **127,** 909–937.

Nan, S., P. Zhao, S. Yang, and J. Chen, 2009: Springtime tropospheric temperature over the Tibetan Plateau and evolutions of the tropical Pacific SST. *J. Geophys. Res.,* **114,** D10104, doi:10.1029/2008JD011559.

North, G., T. L. Bell, and R. F. Cahalan, 1982: Sampling errors in the estimation of empirical orthogonal functions. *Mon. Wea. Rev.,* **110,** 699–706.

Reynolds, R. W., T. M. Smith, C. Liu, D. B. Chelton, K. S. Casey, and M. G. Schlax, 2007: Daily high-resolution blended analyses for sea surface temperature. *J. Climate,* **20,** 5473–5496.

Sun, B.-M., and C.-Y. Li, 1997: Relationship between the disturbances of East Asian trough and tropical convective activity in boreal winter (in Chinese). *Chin. Sci. Bull.,* **42,** 500–504.

Sun, C., and S. Yang, 2012: Persistent severe drought in southern China during winter–spring 2011: Large-scale circulation patterns and possible impacting factors. *J. Geophys. Res.,* **117,** D10112, doi:10.1029/2012JD017500.

Tamura, T., K. Taniguchi, and T. Koike, 2010: Mechanism of upper tropospheric warming around the Tibetan Plateau at the onset phase of the Asian summer monsoon. *J. Geophys. Res.,* **115,** D02106, doi:10.1029/2008JD011678.

Trenberth, K. E., and L. Smith, 2009: Variations in the three-dimensional structure of the atmospheric circulation with different flavors of El Niño. *J. Climate,* **22,** 2978–2991.

Wang, B., Z. Wu, C.-P. Chang, J. Liu, J. Li, and T. Zhou, 2010: Another look at interannual to interdecadal variations of the East Asian winter monsoon: The northern and southern temperature modes. *J. Climate,* **23,** 1495–1512.

Watanabe, M., 2004: Asian jet waveguide and a downstream extension of the North Atlantic Oscillation. *J. Climate,* **17,** 4674–4691.

Webster, P. J., V. O. Magana, T. N. Palmer, J. Shukla, R. A. Tomas, M. Yanai, and T. Yasunari, 1998: Monsoons: Processes, predictability, and the prospects for prediction. *J. Geophys. Res.,* **103,** 14 451–14 510.

Wen, M., S. Yang, A. Kumar, and P. Zhang, 2009: An analysis of the large-scale climate anomalies associated with the snowstorms affecting China in January 2008. *Mon. Wea. Rev.,* **137,** 1111–1131.

Wu, G., Y. Liu, B. He, Q. Bao, A. Duan, and F.-F. Jin, 2012: Thermal controls on the Asian summer monsoon. *Sci. Rep.,* **2,** 404, doi:10.1038/srep00404.

Wu, R., and B. P. Kirtman, 2007: Observed relationship of spring and summer East Asian rainfall with winter and spring Eurasian snow. *J. Climate,* **20,** 1285–1304.

——, Z.-Z. Hu, and B. P. Kirtman, 2003: Evolution of ENSO-related rainfall anomalies in East Asia. *J. Climate,* **16,** 3742–3758.

——, Z. Wen, S. Yang, and Y. Li, 2010: An interdecadal change in southern China summer rainfall around 1992/93. *J. Climate,* **23,** 2389–2403.

Wu, Z., Z. Jiang, J. Li, S. Zhong, and L. Wang, 2012a: Possible association of the western Tibetan Plateau snow cover with the decadal to interdecadal variations of northern China heat wave frequency. *Climate Dyn.,* **39,** 2393–2402.

——, J. Li, Z. Jiang, and T. Ma, 2012b: Modulation of the Tibetan Plateau snow cover on the ENSO teleconnections: From the East Asian summer monsoon perspective. *J. Climate,* **25,** 2481–2489.

Xie, P., and P. A. Arkin, 1997: Global precipitation: A 17-year monthly analysis based on gauge observations, satellite estimates, and numerical model outputs. *Bull. Amer. Meteor. Soc.,* **78,** 2539–2558.

Yang, S., K.-M. Lau, and K.-M. Kim, 2002: Variations of the East Asian jet stream and Asian–Pacific–American winter climate anomalies. *J. Climate,* **15,** 306–325.

——, ——, S.-H. Yoo, J. L. Kinter, K. Miyakoda, and C.-H. Ho, 2004: Upstream subtropical signals preceding the Asian summer monsoon circulation. *J. Climate,* **17,** 4213–4229.

Yu, R., B. Wang, and T. Zhou, 2004: Tropospheric cooling and summer monsoon weakening trend over East Asia. *Geophys. Res. Lett.,* **31,** L22212, doi:10.1029/2004GL021270.

Zhang, L., and T. Zhou, 2012: The interannual variability of summer upper-tropospheric temperature over East Asia. *J. Climate,* **25,** 6539–6553.

——, A. Kumar, and W. Wang, 2012: Influence of changes in observations on precipitation: A case study for the Climate Forecast System Reanalysis (CFSR). *J. Geophys. Res.,* **117,** D08105, doi:10.1029/2011JD017347.

Zhao, P., Z. Zhou, and J. Liu, 2007a: Variability of Tibetan snow and its associations with the hemispheric extratropical circulation and East Asian summer monsoon rainfall: An observational investigation. *J. Climate,* **20,** 3942–3954.

——, Y. N. Zhu, and R. H. Zhang, 2007b: An Asian–Pacific teleconnection in summer tropospheric temperature and associated Asian climate variability. *Climate Dyn.,* **29,** 293–303.

——, J. Chen, D. Xiao, S. Nan, Y. Zou, and B. Zhou, 2008: Summer Asian–Pacific Oscillation and its relationship with atmospheric circulation and monsoon rainfall. *Acta Meteor. Sin.,* **22,** 455–472.

——, S. Yang, and R. Yu, 2010: Long-term changes in the rainfall over eastern China and associated atmospheric circulation under the global warming scenario. *J. Climate,* **23,** 1544–1562.

Zhou, L.-T., C.-Y. Tam, W. Zhou, and J. C. L. Chan, 2010: Influence of South China Sea SST and the ENSO on winter rainfall over South China. *Adv. Atmos. Sci.,* **27,** 832–844.

Zuo, Z., S. Yang, A. Kumar, R. Zhang, Y. Xue, and B. Jha, 2012: Role of thermal condition over Asia in the weakening Asian summer monsoon under global warming background. *J. Climate,* **25,** 3431–3436.